Appl Phys B (2009) 97: 701–713
DOI 10.1007/s00340-009-3713-7

Applied Physics B
Lasers and Optics

Remote sensing with intense filaments enhanced by adaptive optics

J.-F. Daigle · Y. Kamali · M. Châteauneuf · G. Tremblay · F. Théberge · J. Dubois · G. Roy · S.L. Chin

Received: 9 March 2009 / Revised version: 21 July 2009 / Published online: 15 September 2009

Abstract A method involving a closed loop adaptive optic system is investigated as a tool to significantly enhance the collected optical emissions, for remote sensing applications involving ultrafast laser filamentation. The technique combines beam expansion and geometrical focusing, assisted by an adaptive optics system to correct the wavefront aberrations. Targets, such as a gaseous mixture of air and hydrocarbons, solid lead and airborne clouds of contaminated aqueous aerosols, were remotely probed with filaments generated at distances up to 118 m after the focusing beam expander. The integrated backscattered signals collected by the detection system (15–28 m from the filaments) were increased up to a factor of 7, for atmospheric N_2 and solid lead, when the wavefronts were corrected by the adaptive optic system. Moreover, an extrapolation based on a simplified version of the LIDAR equation showed that the adaptive optic system improved the detection distance for N_2 molecular fluorescence, from 45 m for uncorrected wavefronts to 125 m for corrected.

PACS 42.62.Fi · 42.68.wt · 95.75.Qr

J.-F. Daigle (✉) · Y. Kamali · S.L. Chin
Centre d'Optique, Photonique et Laser (COPL) & Département de Physique, de Génie Physique et d'Optique, Université Laval, Québec, Québec G1V 0A6, Canada
e-mail: jean-francois.daigle.2@ulaval.ca

M. Châteauneuf · F. Théberge · J. Dubois · G. Roy
Defense Research and Development Canada (DRDC), Valcartier, Québec G3J 1X5, Canada

G. Tremblay
AEREX Avionique Inc., Breakeyville, Québec G0S 1E1, Canada

1 Introduction

In recent years, due to environmental issues such as global warming [1] and air quality in industrial neighborhoods, there has been an increasing interest towards the development of new tools to control, monitor and quantify pollutants' species released by the different sources. Several laser based methods including remote nanosecond laser-induced breakdown spectroscopy (ns-LIBS) [2] and differential absorption LIDAR (DiAL) [3] have been tested.

Laser filamentation [4–8] resulting from the propagation of intense ultrashort light pulses in air has been proposed as a potentially useful remote sensing tool. In fact, similar to ns-LIBS [2], the high intensity inside the filament core provides simultaneous detection of multiple components present in the target [9, 10]. Moreover, due to the nonlinear behavior of the laser pulse during atmospheric propagation, the technique is less affected by the diffraction limitation. Indeed, filaments have been observed few kilometers from the laser source [11].

In the atmosphere the filaments appear as a dynamic equilibrium between Kerr self-focusing and defocussing by the self-generated low-density plasma produced by multiphoton/tunnel ionization of the air molecules [7]. Indeed, for a non-uniform laser intensity distribution (Gaussian, for example) with peak power higher than the critical power for self-focusing [12], the Kerr effect will act as a lens that will focus the light pulse until its intensity increases beyond the medium's ionization threshold. Once the plasma is sufficiently dense to counteract the Kerr lens effect, the laser pulse will start to defocus. The defocussing nature of the plasma limits and stabilizes the light intensity in each of the filaments. In air, the clamped intensity is approximately 5×10^{13} W/cm^2 [13, 14] and is sufficiently high to ionize any atmospheric constituent or contaminant.

Based on the success of this laser source for atmospheric LIDAR [3, 15] remote sensing applications, Chin et al. claimed in a recent review paper [10] that the high intensity inside a filament core could be used to detect and identify all chemical and biological sample placed on its path. As examples, they mentioned that the technique was successful to detect and identify, via spectroscopic methods, solid metallic and biological targets, gas mixtures, contaminated aqueous aerosol clouds and smoke clouds.

However, as the sensing distance (R) is increased, the LIDAR equation [3] states that the returned signal collected by the detector will be reduced, in ideal and fixed conditions, by a factor $1/R^2$. Therefore, in order to amplify the signal collected, the emissions have to be enhanced by either increasing the initial pulse energy or the effective area of the collecting optics. The second solution can result in an expensive and bulky system. Increasing the pulse energy would, theoretically with a perfectly Gaussian intensity profile, lead to single filament elongation. However, high power laser pulses emitted from an amplifier have relatively large diameters to avoid any damage to the compressor's grating and any inhomogeneities from the gain medium induced small hot spots in the spatial beam profile. Thus, an increase in the pulse energy will deteriorate the quality of the pulse's intensity spatial profile. Each hot zone will tend to self-focus into a filament, competing for the pulse's limited energy. This phenomenon is known as multiple filamentation competition [16]. Multiple filaments that result from such relatively large diameter laser pulses will compete for the energy inside the limited reservoir of the pulse leading to many low plasma density structures inefficient for remote sensing purposes. Hence, the development of techniques for efficient control of filamentation at long distances is necessary for remote applications.

Several methods of filamentation control using laser pulses with many times the critical power in air have been proposed [17–19], but since the scope of this paper aims towards wavefront control, only the techniques involving wavefront modifications will be discussed.

The simplest wavefront modification used to enhance the plasma produced by filaments consists in using a converging optic to focus the laser pulses [20]. For filaments produced near the geometrical focus of a short focal length lens, the generated plasma density inside the filament required to defocus the laser pulse will be enhanced to balance, similarly to a lens combination effect, the added geometrical wavefront curvature. Thus, as the focusing distance increases, the filament's plasma density decreases.

Such behavior is not appropriate for remote sensing application. The technique proposed to counteract these effects combined beam expansion, which prevented early multiple filaments by increasing the self-focusing distance of the wavefront's hot zones, and geometrical focusing of the laser pulses at a remote location [21, 22]. Because of the hot spots' larger diameter, the created filaments were induced near the geometrical focus and lead to the generation of a strong plasma at a localized position. In the case of long distance focusing, which is normally associated with a weaker wavefront curvature, the plasma enhancement is not attributed to the increased plasma density induced by the added wavefront curvature. The main advantage of geometrical focusing, as opposed to free propagation, is that, near the focal point, the confinement of the energy reservoir allows for optimal energy feeding of larger and more powerful multiple laser filaments which in turn provide a larger quantity of ionized molecules or atoms.

Some methods also involved adaptive optic systems. Indeed, based on an idea initially proposed by the *Teramobile* [23], Jin et al. used a deformable mirror to delay the onset of filaments by changing the initial divergence of the laser pulses [24]. They demonstrated that the collapse position increased with the beam divergence. Recently, it has been suggested that an adaptive optic (AO) system inserted in a focusing beam expander could be used to adequately deliver ultrashort pulses at a remote location to efficiently generate strong filaments [25]. The deformable mirror used was unimorph, had 16 actuators and a rest curvature of -70 cm. Strong N_2 signals, detected with a photomultiplier tube (PMT) based LIDAR, were collected from filaments formed 75 m away from the focusing beam expander.

In this paper, we demonstrate that the filaments produced by a similar device (AO-focusing beam expander) can be used for remote sensing applications to enhance the backscattered signal collected by the detector. The technique has been tested on multiple targets probed at a distance ranging from 107 m to 118 m from the focusing beam expander. The plasma emissions produced from the interaction of filaments with gases (Air and Air + CH_4), solid metallic targets (Pb) and contaminated airborne aqueous aerosols (NaCl dissolved in H_2O), was collected and identified using a spectrometer based LIDAR.

2 Experiment

2.1 Adaptive optic system (Night N (opt) [26])

The adaptive optics [27] consists of a flat, bimorph deformable mirror (DM) of 55 mm diameter (Fig. 1). Two superposed piezoceramic crystals, which share a common ground at the interface, are fixed under a glass substrate whose other surface is coated for high reflectivity at 800 nm at normal incidence. The DM's maximal deformation is characterized by a stroke of 40 μm. The top piezo-disc, which is activated by a circular electrode (E1) sandwiched between the substrate and the disc, serves as curvature deformation of the mirror. If the beam is properly centered on its

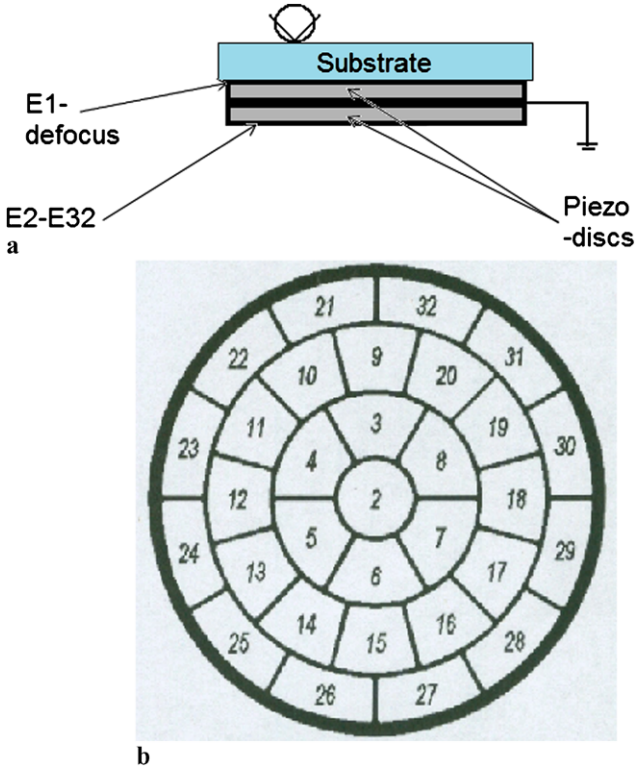

Fig. 1 (**a**) Schematics of the deformable mirror's construction. (**b**) Disposition of the electrode pattern on the lower surface of the deformable mirror

surface, it will only affect the general defocus of the beam. The lower disc is subdivided into 31 actuators (E2–E32) determined by an array of activation electrodes located at the assembly's bottom. These actuators will correct for general wavefront aberrations measured by the wavefront sensor (WFS).

The wavefront sensing device used for this experiment is of type Shack–Hartmann [27]. It consists of an array of lenslets of the same focal length (size of array: 40×40, $\text{diameter}_{\text{lenslet}} = 250$ µm, $\text{focal}_{\text{lenslet}} = 14$ mm). A CMOS detector chip is located at the focal plane of the lenslet array. The local tilt of the wavefront across each lens can then be calculated from the position of the focal spot on the sensor. Any phase aberration can be approximated by a set of discrete tilts. By sampling an array of lenslets which corresponds to the beam area, all of these tilts can be measured and used to reconstruct the wavefront phase distribution.

The two components work in a closed loop system which automatically drives the DM's actuators until the WFS observes a flat wavefront. This flat wavefront is associated to a Shack-Hartmann reference pattern obtained from a collimated light beam of wavelength and diameter close to the operation conditions, uploaded in the software. Any local phase shift is measured and calculated with respect to this reference.

Before the automated correction is activated, the wavefront response of each DM's actuator associated to a specified voltage is measured and stored in the software. These responses are then used by the closed loop system as basic elements for the wavefront correction. Each time the alignment of the adaptive optic system is modified, this response measurement has to be repeated. The closed loop correction system is triggered at a 10 Hz repetition rate with the laser pulses incident on the CMOS detector. The system's maximal repetition rate is mainly limited by the wavefront measurement, which takes approximately 33 ms, and the correction via the application of voltages to the electrodes, which takes 17 ms. Therefore, the overall response time is 50 ms which corresponds to a 20 Hz maximal repetition rate that is twice that of the laser pulse train.

2.2 Focusing beam expander

The focusing beam expander used in the experiments is illustrated in Fig. 2. It is composed of a convergent off-axis parabolic mirror (PM) with a metallic coating and a divergent dielectric spherical concave mirror (CM), mounted on a translation stage, coated for high reflectivity at 800 nm. The PM has a diameter of 15 cm and a focal length of 150 cm. With $f_{\text{CM}} = -50$ cm and collimated input and output, the focusing beam expander has a magnification of $3\times$. The output beam diameter, measured at e^{-2} of the maximum intensity profile, is 6.3 cm. Strong aberrations induced by the beam expander mirrors were observed in the output laser.

The closed loop adaptive optic system described earlier was inserted in the focusing beam expander. The WFS was located at the exit of the beam expander behing a reflective wedge. It measured the wavefront of the partial transmission through the reflective wedge. The DM used to correct the wavefront was placed before the convex mirror (CM). Both CM and DM are mounted on a translation stage. A relative motion of CM with respect to PM will change the focal length of the beam expander.

2.3 Experiment outline

For the remote sensing experiments, three different types of targets were selected: gaseous (air, mixture of air and hydrocarbons), solid lead and aqueous aerosols containing metallic ions (droplet composed of H_2O and NaCl). These targets were positioned at various distances ranging from 107 m to 118 m away from PM.

The experimental setup is presented in Fig. 3. Short laser pulses, emitted from a commercial Ti:Sapphire laser system (Spectra-Physics), are directed to the focusing beam expander presented in Fig. 2 and then launched in a 30 m long corridor. In order to provide significant propagation length ($\approx$120 m), the laser beam was folded 3 times with coated dielectric mirrors positioned at the corridor's extremities. The

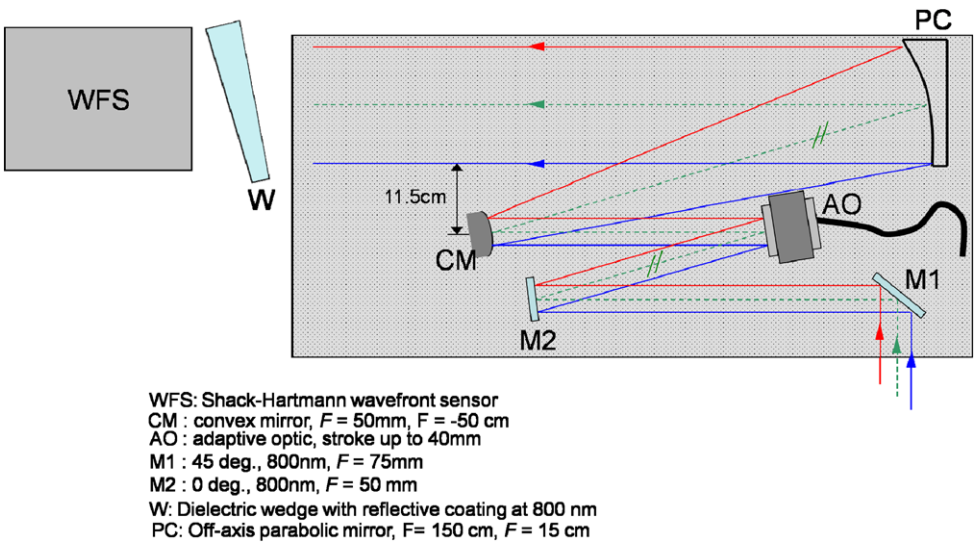

Fig. 2 Schematics of the focusing beam expander and adaptive optic system

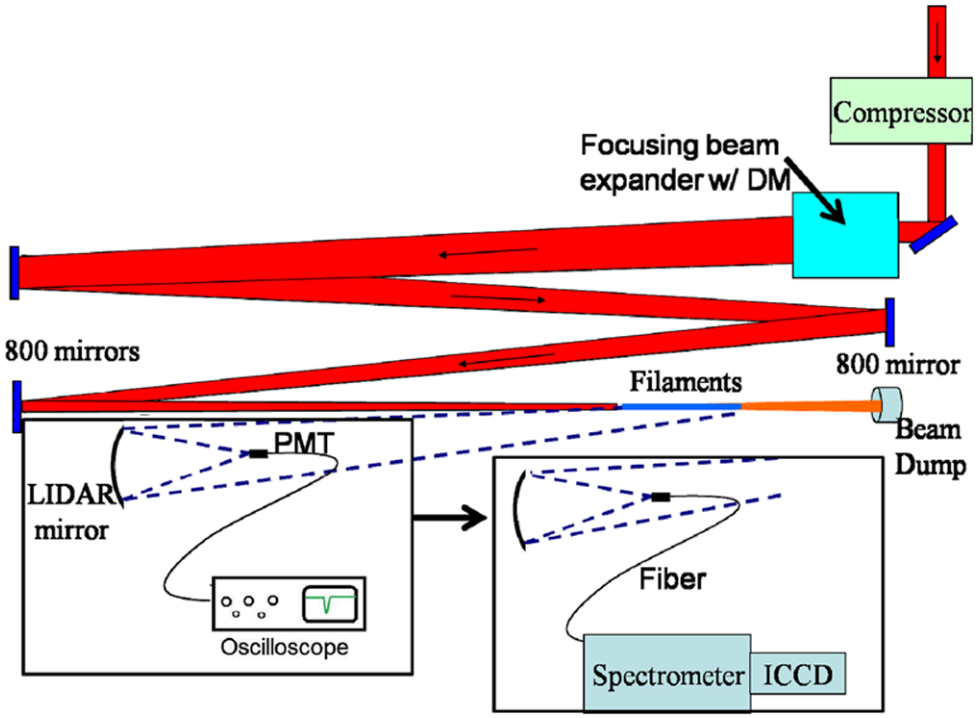

Fig. 3 Experimental setup for remote sensing experiments using the adaptive optic system. Pulses were sent in a 30 m long corridor that provided 120 m long propagation (3 folds). The signals were collected by a LIDAR system

focusing beam expander's focal length was set to approximately 120 m. Initially, the WFS was positioned as shown in Fig. 2. However, the reflections on the wedge's surface and, on the folding mirrors at the corridor's ends, provided a significant amount of distortion to the wavefront. In fact, the surface quality of these reflectors was characterized with a Zygo interferometer [28] and the average root-mean-square (rms) deformation corresponded to 0.35 μm. These added deformations ($4 \times \text{rms} = 1.4$ μm) were not measured by the WFS located at the output of the beam expander and hence were not corrected by the AO system. This added uncorrected deformation combined with the long propagation distance deteriorated the focal volume and, even with the AO system operating, no significant filamentation was observed at the targets' location. In order to correct part of these deformations, the WFS was positioned behind the dielectric mirror located 60 m after the focusing beam expander. In a real remote sensing application, it would be impossible to put the WFS at this position, however, since the folding mirror are major source of aberration and they will not be used in a real application, we still believe that the following results demonstrate the application's feasibility.

To characterize the wavefront's aberrations, the WFS' software computes the various Zernike polynomials. For

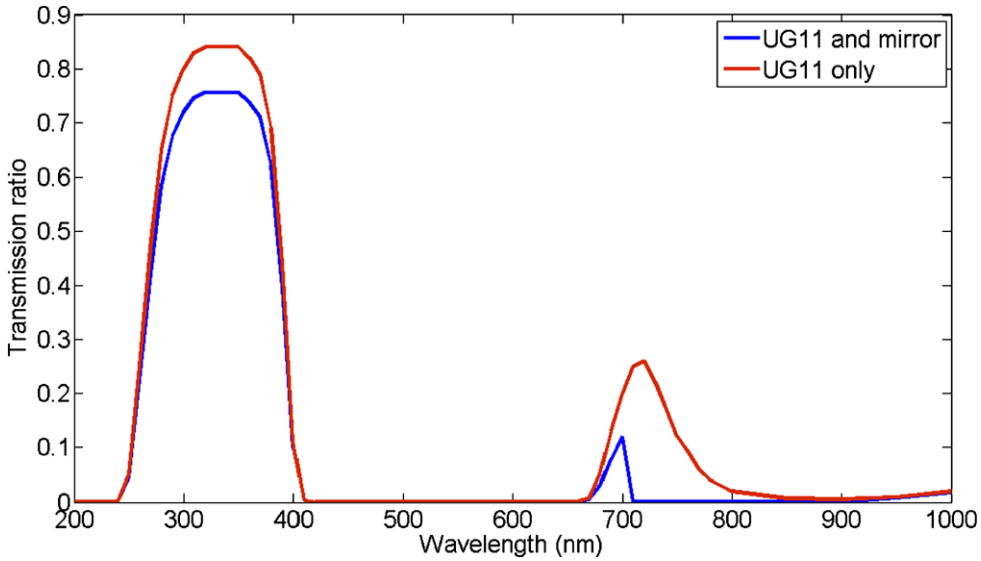

Fig. 4 Spectral transmission curves measured using a commercial spectrophotometer for the UG11 filter alone and when a mirror with high reflectivity at 800 nm is added

each focal distance of the focusing beam expander, the measured wavefront curvature associated to the defocus Zernike polynomial (Z_2^0) was eliminated. This operation was carried out, without altering the values corresponding to the other Zernike polynomials, with a modification of the distance between the two WFS' imaging optical elements. Therefore, the wavefront curvature and the focusing beam expander's focal distance were not affected by the AO system's correction. Moreover, the defocus actuator (E1 on Fig. 1a) is not activated during the automatic correction; therefore, no additional curvature is added. The uncorrected wavefronts were mostly characterized with aberrations of type astigmatism (1.3 μm/1.6 wavelength along the 0°–90° (Z_2^2) and 0.3 μm/0.4 wavelength along the ±45° (Z_2^{-2})). The other Zernike polynomials, corresponding to the other type of aberrations were negligible. When the wavefront correction is activated, these Zernike values for astigmatism drop considerably (30 nm/0.03 wavelength) and the measured wavefront can be considered has being almost flat.

The signals were collected from the other end of the corridor (i.e. about 20–30 m from the filament zone) with a 25 cm diameter LIDAR mirror of 150 cm focal length and focused onto a detector. In Fig. 3, a PMT tube covered by a UG11 filter [29], used as bandpass filter for atmospheric N_2 fluorescence, allows for the characterization of the filament longitudinal plasma distribution. A dielectric mirror with high reflectivity at 800 nm was used in front of the UG11 to remove most of the scattered 800 nm laser light. To ensure that only N_2 fluorescence is detected throughout the measurement, the transmission curves, presented in Fig. 4, for UG11 only (red) and the UG11/mirror assembly (assembly) were measured using a commercial spectrophotometer. The addition of the dielectric mirror eliminates the major part of the transmission band located between 675 to 830 nm, where a possible contamination of the supercontinuum could have occurred. However, as we will see further down the text, the supercontinuum generated using the present configuration spans the spectral region between 760 to 840 nm (Fig. 8) where the measured transmission of the UG11/mirror assembly is very close to zero (10^{-5}).

For the other targets (inset of Fig. 3), the collected light was focused onto a fiber bundle and delivered to a spectrometer coupled to a gated intensified CCD (ICCD). The LIDAR positioning at the 90 m position was forced by the 3-fold propagation configuration.

3 Results

3.1 Beam patterns close to the focal distance

The beam's intensity profiles, measured 120 m away from the focusing beam expander (close to its geometrical focal position), are presented in Fig. 5 for (a) uncorrected and (b) corrected wavefronts. A CCD camera covered by a 800 nm bandpass filter was used to image the pulses scattered by a white sheet of paper. Since the screen was close to the focal area, filaments were avoided by using negatively chirped pulses of 5 ps (duration$_{\text{Transform limited}} = 45$ fs) with and an energy of 25 mJ.

The elongated pattern in Fig. 5b indicates that there is some uncorrected astigmatism. It is believed that most of it was induced by the reflections on the mirrors located at 60 m and 90 m, which could not be compensated by the AO system.

3.2 Remote sensing of N_2 in air

The AO system was first tested to measure N_2 emissions from ambient air in the laboratory. The PMT based LIDAR

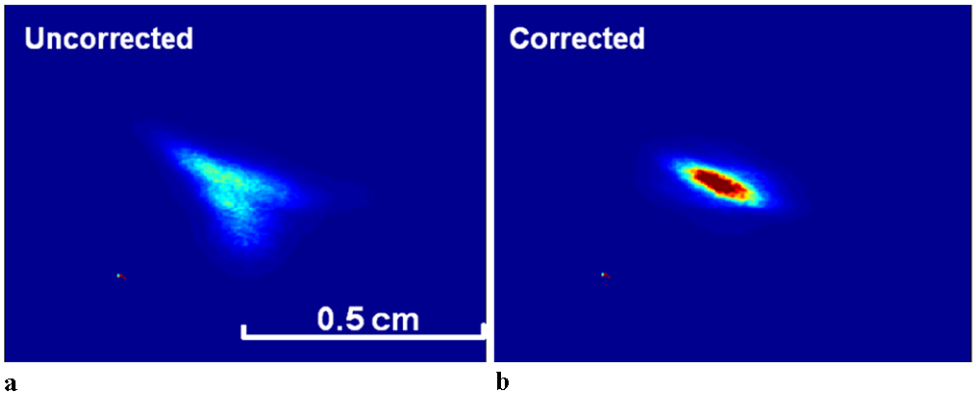

Fig. 5 Beam Patterns measured 120 m after the focusing beam expander for uncorrected and corrected laser pulses without self-focusing/filamentation

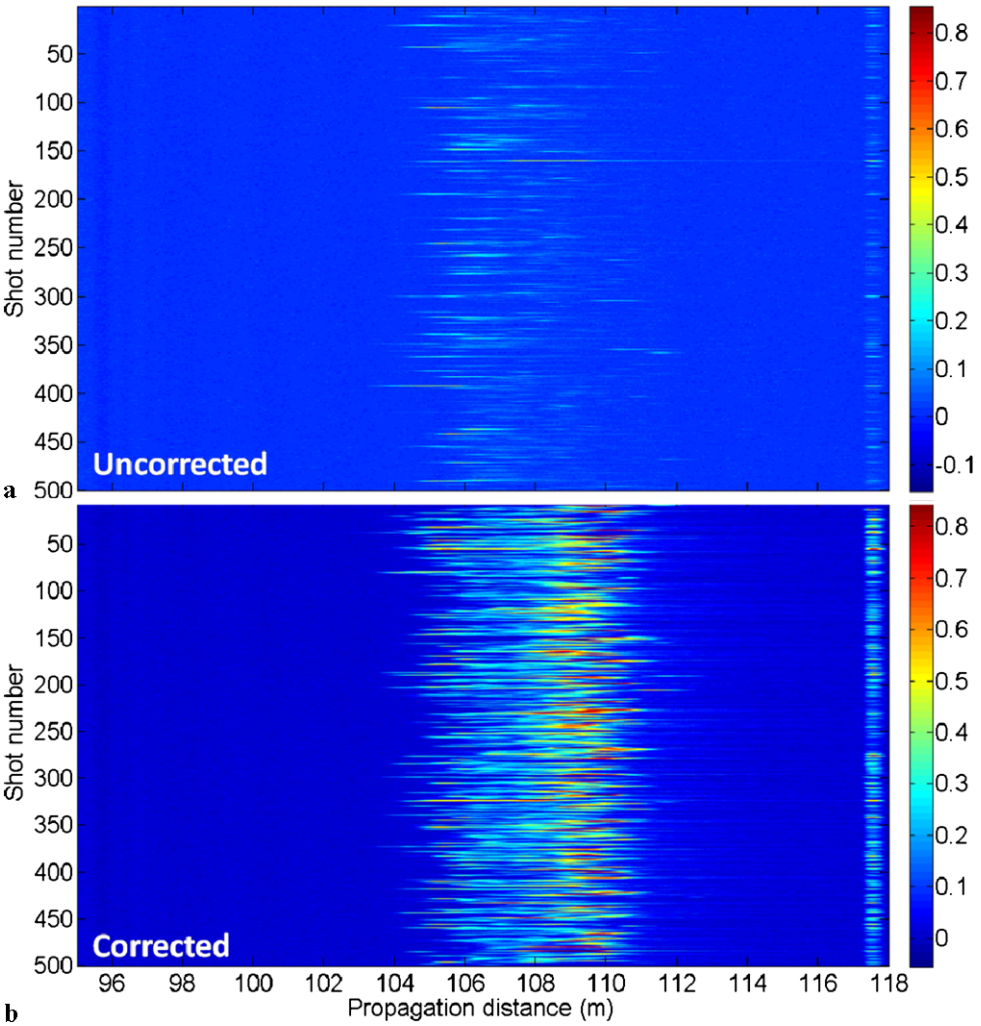

Fig. 6 Backscattered N_2 emissions signals measured, with a PMT based lidar, for uncorrected and corrected wavefronts. The signal close to 118 m corresponds to the supercontinuum scattered on the beam dump

configuration shown in Fig. 3, has been used to characterize the plasma distribution of the formed filaments for the case of uncorrected and corrected wavefronts. The pulse energy was 70 mJ and the pulse duration was set to 3 ps, negatively chirped.

Figure 6 presents, for (a) uncorrected and (b) corrected wavefronts, 500 backscattered traces from individual laser shots. Each plot has for horizontal scale the distance from the focusing beam expander, the vertical scale corresponds to the number of the trace recorded and the color scale is the N_2 signal intensity. This plot shows that both the amount of signal produced by the filaments and the consistency of filament generation are improved when the wavefront correction is applied.

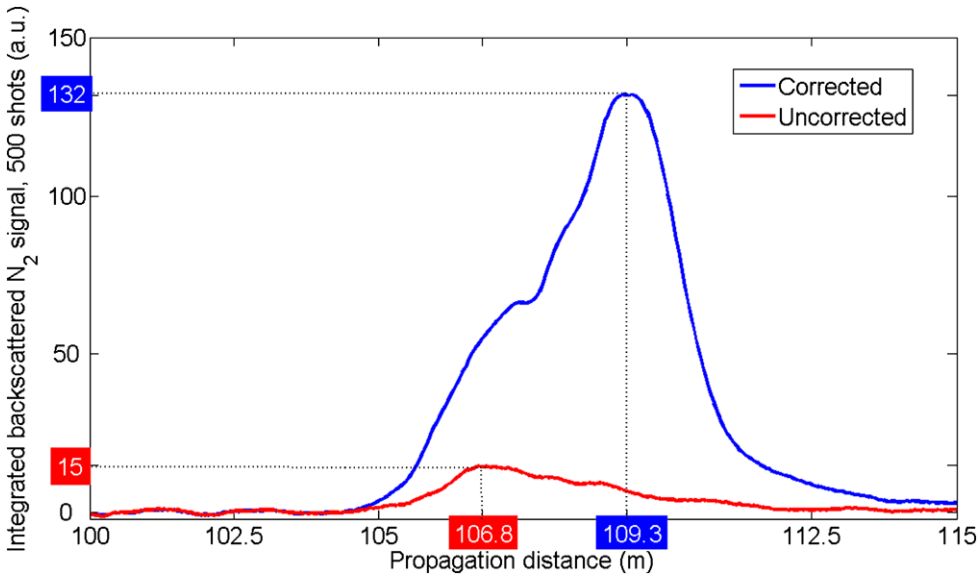

Fig. 7 The 500 traces presented in Fig. 6 are summed and presented as a single plot. The integrated backscattered signal is enhanced 7 times for corrected wavefronts

The two curves presented in Fig. 7 correspond to the sum of the 500 traces shown in the previous Figure for the uncorrected and corrected wavefronts. The AO system improved the overall integrated signal is enhanced 7 times. The shoulder observed on the corrected curve is attributed to a shot-to-shot fluctuation of the correction applied by the AO system. Indeed, it seems that some laser pulses, which could not be corrected properly, collapsed at a shorter distance (∼107 m). The fact that the shoulder roughly corresponds to the uncorrected signal's maximum position enforces this argumentation.

The PMT setup was replaced by the spectrometer/ICCD assembly, as shown in Fig. 3, and the spectra of air were taken. In order to get enough signals from the ICCD, the pulse energy was increased to 85 mJ and its duration shortened to 2 ps, negatively chirped. The gated detector was trigged 1 ns before the formation of the filaments and the gate window was opened for 30 ns. The spectra in Fig. 8 are the result of 100 accumulated laser shots for the case of (a) uncorrected and (b) corrected wavefronts. When the AO system was turned off (Fig. 8a), only the fundamental pulse scattered on the beam dump could be measured. This indicates that the signal observed with the PMT in Fig. 6a is very weak N_2 signals which could not be detected, because of its lower detection efficiency (∼70% that of the PMT/filters), by the fiber/spectrometer/ICCD assembly. This reduced efficiency is mainly attributed to the spectrometer's diffraction grating which separates the different spectral components while the PMT/filters assembly integrates over the entire spectrum. When the AO system was used, strong N_2 bands were observed. The previous results indicate that the wavefront correction has a strong effect on remote sensing of atmospheric gas samples.

3.3 Remote sensing of hydrocarbons in air

Three hydrocarbon gases, namely methane (CH_4), acetylene (C_2H_2) and ethylene (C_2H_4), were tested. Each sample consisted of a mixture of 2% of hydrocarbon gas balanced to atmospheric pressure with air. The mixture was then injected into a 2 m long metallic tube with open ends which was placed at the filaments' zone (110 m after the focusing beam expander). The middle part of the pipe had an exit which was connected to the ventilation to ensure a continuous renewal of the gas mixture. The energy of the laser was 85 mJ with a pulse width of 2 ps negatively chirp. One after the other, the gases mixtures were injected in the tube and the CH emissions, resulting from the interaction with the filaments, were recorded.

The spectra of pure air (red) and contaminated air (black) are presented in Fig. 9 for (a) 2% C_2H_2, (b) 2% C_2H_4 and (c) three different concentrations of CH_4. Because no signals could be obtained without wavefront correction, spectra 8a-c were measured with an active AO system. At 2% concentration, the CH band could be detected and identified for all the tested gas mixtures and the strongest CH signal was obtained in C_2H_2 (Fig. 9a). As shown in Fig. 9c, three different concentrations of methane mixtures were available and tested. Even at the lowest available concentration, 0.5% CH_4 in air, the CH emission band could be identified, and an extrapolation of the integrated CH signal indicates that, in these experimental conditions, the minimal concentration of methane that could be measured, at this 20 m distance, would be approximately 0.34%.

3.4 Lead

The gas tube was then replaced by a lead target mounted on a rotating motor located 118 m after the focusing beam

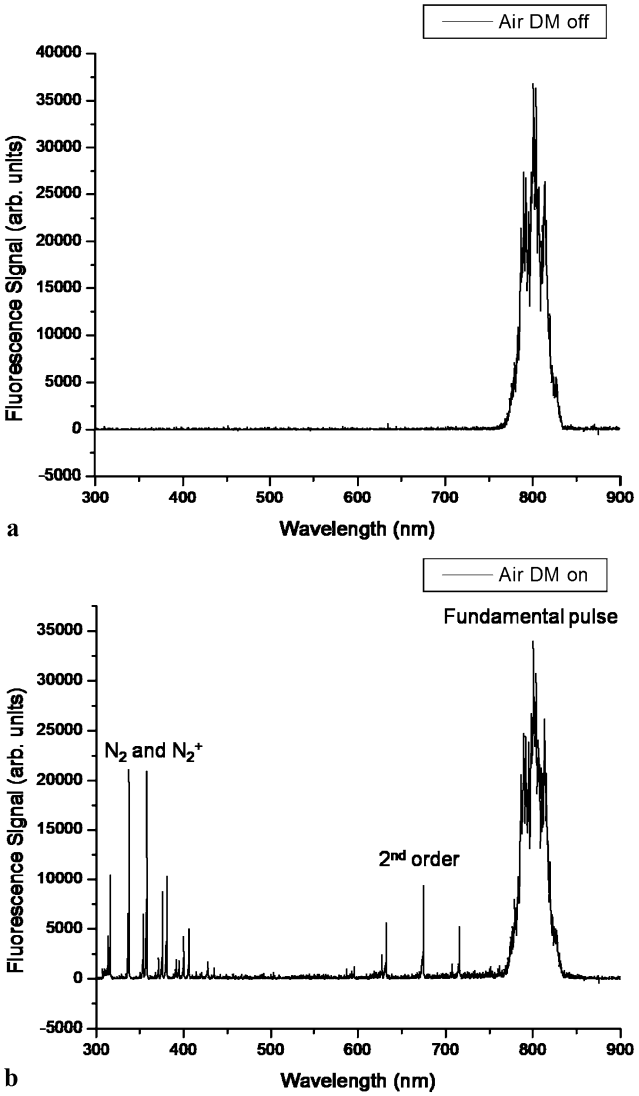

Fig. 8 Backscattered spectra measured with the spectrometer/ICCD assembly, for **a** uncorrected and **b** corrected wavefronts

expander. The focal length of the device was adjusted to obtain a strong filament interaction at the target's location. The sample's rotation ensured that each oncoming laser pulse hit on a fresh surface. In order to avoid signal degradation due to surface deterioration, the sample's surface was cleaned with a sharp blade before each spectral measurement.

Filaments, formed from 80 mJ/5 ps negatively chirped laser pulses, interacted with the sample and the recorded spectra are shown in Fig. 10 for uncorrected and corrected wavefronts. The temporal gate was opened for 100 ns, triggered 2 ns after the pulse interaction with the target. These results show that, when the wavefront correction is applied, the integrated (350 to 575 nm) backscattered signal increases by a factor 6.8. It demonstrates the efficiency of the AO system to increase the backscattered emissions from metallic targets.

3.5 Aerosols

The last target used in this series of experiments consisted of an aqueous aerosol cloud in which NaCl was dissolved at a concentration of 5 g_{NaCl}/L_{water}. Aerosols were generated by a commercial ultrasonic humidifier (Sunbeam, Health at home), which produces droplets of 10 μm mean diameter, and injected in a mobile aerosol chamber. The microdroplet density is approximately 300 cm^{-3} [30]. An exhaustive description of the aerosol chamber has already been published [30].

Filaments formed from the 80 mJ/5 ps negatively chirped laser pulses interacted with the target located 110 m away from the focusing beam expander. The backscattered sodium emissions, measured with the spectrometer/ICCD assembly, are presented in Fig. 11 for (a) uncorrected and (b) corrected wavefronts.

In both scenarios, the sodium doublets were easily identified. As expected, the integrated (588.0 to 591.5 nm) backscattered signal increased when corrected wavefronts generated the filaments. In fact, the intensity at the core of a grown filament in air is sufficiently high to explode the microdroplet and significantly contribute to enhance the emissions [30].

However, this enhancement factor (2.3) is not as important as the other targets, because the ionization mechanism does not entirely rely on filamentation in air. In fact, the aqueous aerosol cloud can be thought of as a cloud of micron size and randomly distributed spherical lenses [31]. Each small lens can focus the incident light to nanosized regions, within the microdroplets, to produce a plasma and, fingerprint emissions. Indeed, when an ultrashort laser pulse meets a microdroplet contaminated with NaCl, the light coupling mechanism takes place and Na emissions are produced. As a result, the signal is already strong for uncorrected wavefronts and any enhancement due to filaments formed from the corrected wavefronts becomes limited.

4 Discussion

4.1 The effects of external focusing

Using geometrical optics and Rayleigh diffraction formalism, it is possible to evaluate the maximal focal intensity provided by laser pulses focused linearly with the focusing beam expander. In this approximation, the effects of self-focusing, group velocity dispersion and ionization are neglected. Because of linear diffraction, the minimal focal beam diameter (d) obtained from a focused Gaussian beam is determined by the equation:

$$d = \frac{\lambda_f}{\pi D} \tag{1}$$

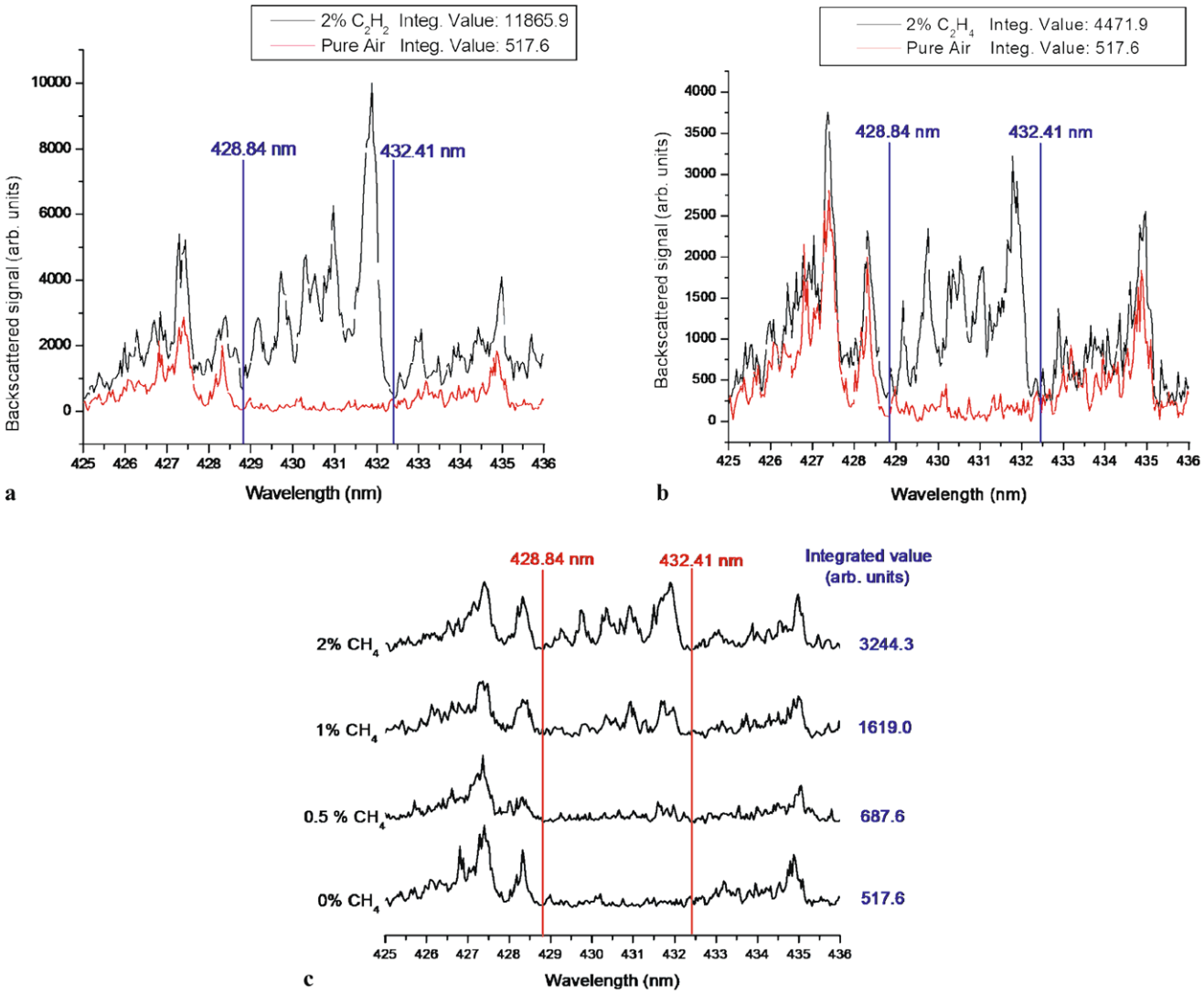

Fig. 9 Filament emissions spectra of **a** pure air (*red*) and contaminated with 2% C_2H_2 (*black*). **b** pure air (*red*) and contaminated with 2% C_2H_4 (*black*) and **c** CH_4 in different concentrations of 0 to 2%. Integrated values of the CH cand between 428.84 to 432.41 nm are used to characterize the hydrocarbon signal strength

where λ corresponds to the pulse's wavelength, f is the focal length and D the beam diameter at the optical element's output. Therefore, the focal diameter linearly increases with the focal distance and is inversely proportional to the beam diameter D. The back focal length (BFL) of the focusing beam expander is determined using the following two lens equation

$$\mathrm{BFL} = \frac{f_2(L - f_2)}{L - (f_1 - f_2)} \tag{2}$$

where $f_1 = -50$ cm is the focal length of the focusing beam expander's diverging element, $f_2 = 150$ cm is the focal length of its converging element and L is the distance between the two elements. However, the focal length modification implies a relative displacement of the two optical components which makes D dependent on L and, incidentally, on BFL. Based on basic trigonometric rules and the knowledge of the beam's diameter at the compressor's output ($D_{\mathrm{in}} = 2$ cm at e^{-2}), we find that

$$D = \frac{D_{\mathrm{in}}(f_2 - L)}{f_2} \tag{3}$$

Equations (1)–(3) can be used to determine the equation which gives the maximal linear laser intensity at the focal point (I_{Ray}) as a function of D and BFL:

$$I_{\mathrm{Ray}} = \frac{4\pi P D^2}{\lambda^2 \mathrm{BFL}^2} \tag{4}$$

where P is the initial pulse power. Figure 12 shows the calculated focal intensity as a function of the focusing beam ex-

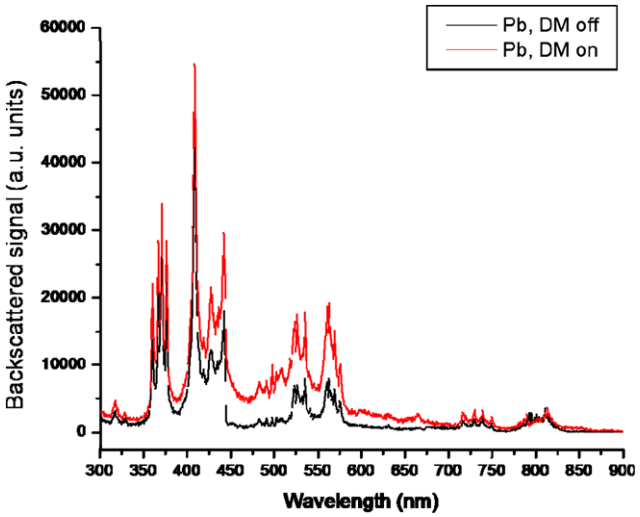

Fig. 10 Typical lead spectra measured for uncorrected (*black*) and corrected (*red*) laser pulses. The integrated lead signals increases by a factor 6.8 for corrected wavefronts

pander's BFL for 80 mJ laser pulses with a chirped duration of 5 ps. The plot demonstrates that with a perfectly focused Gaussian beam, the maximal focal intensity drops below the clamped intensity in air at 50 m, and that at 100 m it drops below its ionization threshold ($\approx 10^{13}$ W/cm^2). Therefore, beyond this distance, geometrical effects can no longer provide ionized air molecules.

A comparison with the patterns presented in Fig. 5 clearly show that the Rayleigh limitation is not attained and that, even when the system AO is active, the focused wavefronts contain a significant amount of aberrations. In fact, it is possible to estimate the linear laser intensity at this position by evaluating the focal area. For this calculation, only the CCD pixels whose count number is higher than e^{-2} times the profile's maximal pixel count are considered. Based on these measurements and considering only linear propagation, the focal intensity for 80 mJ/5 ps uncorrected and corrected laser pulses is, respectively, 9.3×10^{10} and 1.96×10^{11} W/cm^2 (indicated as dots in Fig. 12). Therefore, the AO system has the possibility to increase the linear intensity by a factor 2.

Nevertheless, these values are well below both the Rayleigh intensity limit and the air molecules' ionization threshold which implies that all the gaseous (air, hydrocarbons) fluorescence signals presented arose from the interaction with laser filaments. The geometrical effect provided by the focusing beam expander is not only used to determine the longitudinal positioning of the filaments. More importantly, it confines the pulse's energy reservoir in a small volume, near the focal point, where an optimal feeding of the laser filaments occurs by eliminating the effects of multi-filaments' competition [32]. Therefore, the enhanced fluorescence signal (factor ~7 in air), observed in the case of corrected wavefronts, is not directly caused by an increase of the laser intensity near the focal zone. It is rather attributed to an increased number of filaments sustained by this intense energy reservoir.

However, in the case of aqueous microdroplets and a solid lead target, this argumentation cannot be applied. Indeed, since these samples have lower ionization potentials and higher medium density ($\rho_{\text{water}} \approx 10^3 \rho_{\text{air}}$, $\rho_{\text{Pb}} \approx 10\rho_{\text{water}}$), it is possible, via optical breakdown mechanisms, to excite plasma emissions with pulses which do not form filaments. It is therefore difficult to distinguish whether the signal enhancement is attributed to an increased number of filaments or to the increased focal intensity. Nevertheless, the observation of white light generated through self phase modulation, especially for corrected wavefronts, suggests that filaments were formed before the laser pulse is incident on the target and that their intensity was already stabilized to the air clamped intensity of 5×10^{13} W/cm^2. This enhanced supercontinuum can be observed, for corrected wavefronts, on Figs. 6b (scattered on the beam dump) and 11b (microdroplets' multiple scattering). It is absent in the case of lead because the detector's temporal gate opens after the pulse is incident on the target. The produced supercontinuum would have masked the signal. Therefore, the enhanced signals of lead and sodium are caused by intense filaments formed by the wavefront corrected laser pulses.

4.2 Extrapolation of the air signal

In the current beam-folding configuration, N_2 fluorescence excited by filaments generated 110 m after the focusing beam expander was detected with a LIDAR located ~18 m away from the filament zone. Therefore, an extrapolation based on the LIDAR equation (3) has to be performed to verify whether the produced signal is sufficiently intense to be detected at a distance larger than 110 m. Assuming a perfect scenario where only the detection solid angle dependence is influent, the collected signal will decrease as the square of the distance (R) between the LIDAR and the filaments ($1/R^2$). The traces presented in Fig. 6 are used to extrapolate for the N_2 fluorescence signal collected at a distance of ~18 m for uncorrected and corrected wavefronts. For this calculation, the peak signal intensity is extrapolated, based on the R^{-2} relationship, until it reaches the detection limit which corresponds to the maximum background signal (Fig. 7, 95–102 m) plus 3 times the background standard deviation. The results are presented in Table 1. This simple calculation demonstrates that the signal produced by the uncorrected wavefronts could be observed at a maximal distance of 32 m whereas the corrected ones could reach 125 m. It corresponds to an increase by a factor 3.9.

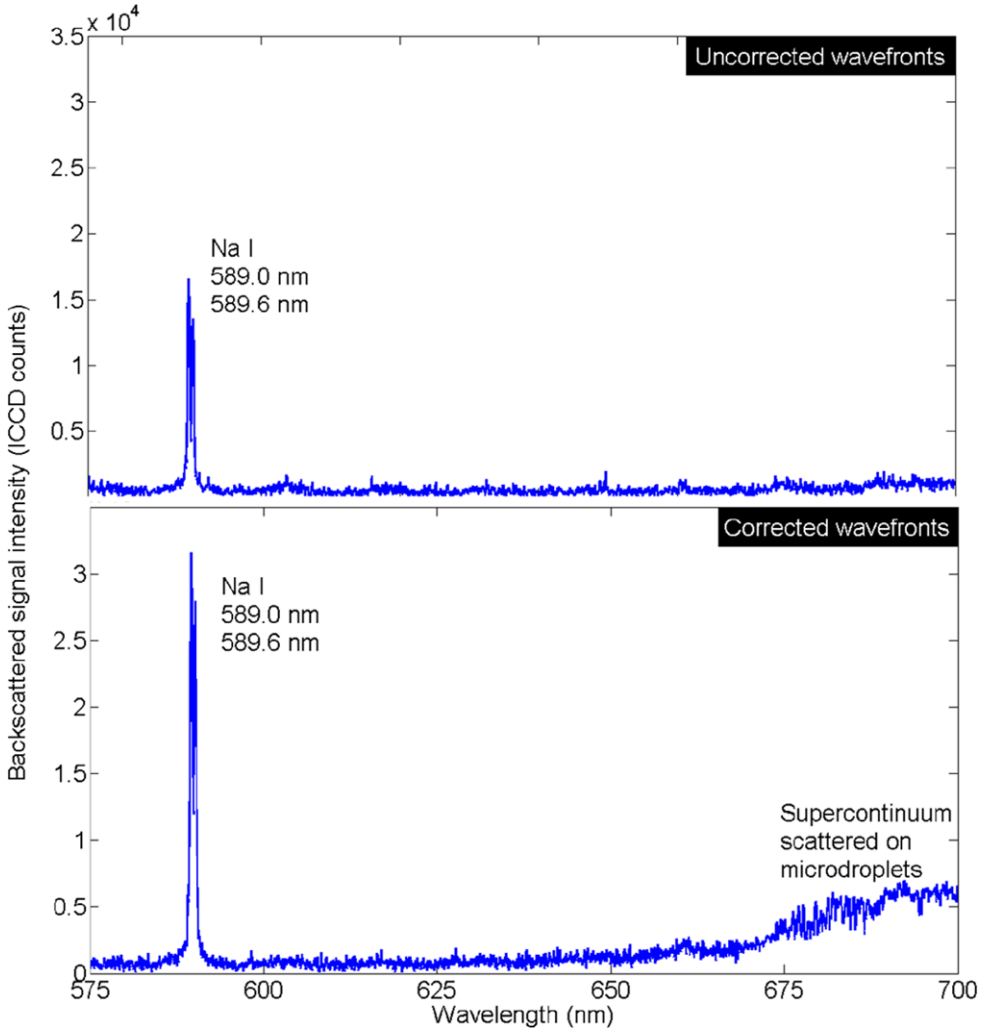

Fig. 11 Typical sodium spectra measured from aqueous aerosol clouds with uncorrected and corrected laser pulses. The integrated sodium emission increases by a factor 2.3 for corrected wavefronts

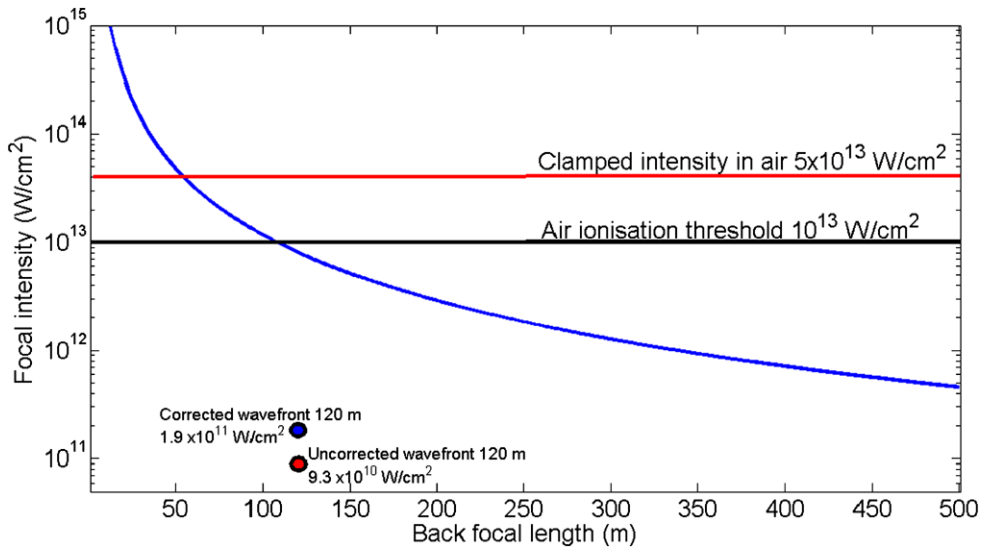

Fig. 12 Evaluation of the linear focal intensity that can be achieved using the actual focusing beam expander and 80 mJ/5 ps (-) chirp pulses. This calculation excludes the effects of self-focusing, ionization and group velocity dispersion. The *blue curve* corresponds to the linear intensity calculated from (4) and the two dots corresponds to the intensity estimations based on the intensity profiles shown in Fig. 5

5 Conclusions

In this paper, we demonstrated that a focusing beam expander assisted by an adaptive optic system could provide significant enhancement of the filament emissions in the case of remote sensing experiments involving filamentation. Moreover, the technique proved to be efficient on multiple targets under different phases: gaseous (Air and Air + CH_4), solid metallic (Pb) and contaminated airborne

Table 1 Details of the extrapolation performed for the backscattered traces presented in Fig. 7

	Uncorrected	Corrected
Peak signal (a.u.)	14.63	132.08
Peak signal distance from LIDAR (m)	16.8	19.3
Detection limit: mean + 3δ (a.u.)	4.2	3.1
Maximum extrapolated distance (m)	32.1	125.3

aqueous aerosols (NaCl dissolved in H_2O). In fact, all the targets probed showed a significant increase of the collected emissions when filaments were formed with wavefront corrected laser pulses (up to a factor 7 for atmospheric N_2). We demonstrated that this enhancement is not directly attributed to the increased intensity at the focal zone. In fact, it is rather attributed to the generation of an increased number of strong filaments sustained by this intense energy reservoir. An extrapolation based on the LIDAR equation showed that the adaptive optic system improved the detection limit by a factor 3.9 when the extrapolated distance for N_2 signal passed from 32 to 125 m, for uncorrected and corrected wavefronts respectively. This quick calculation demonstrates, from another point of view, how the presented system can significantly enhance the backscattered signal and the detection distance, without increasing the pulses' energy and the laser cost.

Acknowledgements This work was partially supported by NSERC, DRDC-Valcartier, Canada Research Chairs, CIPI, CFI, and FQRNT. We appreciate very much the technical assistance of Mr. Mario Martin.

References

1. Emissions trading. United nations framework convention on climate change (2009). http://unfccc.int/kyoto_protocol/mechanisms/emissions_trading/items/2731.php
2. S. Palanco, L.M. Cabalín, D. Romero, J.J. Laserna, Infrared laser ablation and atomic emission spectrometry of stainless steel at high temperatures. Anal. At. Spectrom. **14**, 1883–1887 (1999)
3. R.M. Measures, *Laser Remote Sensing: Fundamentals and Applications* (Krieger, Florida 1992)
4. A. Couairon, A. Myzyrowicz, Femtosecond filamentation in transparent media. Phys. Rep. **441**, 47 (2007)
5. J. Kasparian, J.-P. Wolf, Physics and applications of atmospheric nonlinear optics and filamentation. Opt. Express **16**, 466 (2008)
6. L. Bergé, S. Skupin, R. Nuter, J. Kasparian, J.-P. Wolf, Ultrashort filaments of light in weakly-ionized, optically-transparent media. Rep. Prog. Phys. **70**, 1633–1713 (2007)
7. S.L. Chin, S.A. Hosseini, W. Liu, Q. Luo, F. Théberge, N. Aközbek, A. Becker, V.P. Kandidov, O.G. Kosareva, H. Schroeder, The propagation of powerful femtosecond laser pulses in optical media: physics, applications, and new challenges. Can. J. Phys. **83**, 863–905 (2005)
8. A. Braun, G. Korn, X. Liu, D. Du, J. Squier, G. Mourou, Self-channeling of high-peak-power femtosecond laser pulses in air. Opt. Lett. **20**, 73 (1995)
9. K. Stelmaszczyk, P. Rohwetter, G. Méjean, J. Yu, E. Salmon, J. Kasparian, R. Ackermann, J.-P. Wolf, L. Wöste, Long-distance remote laser-induced breakdown spectroscopy using filamentation in air. Appl. Phys. Lett. **85**(18), 3977 (2004)
10. S.L. Chin, H.L. Xu, Q. Luo, F. Theberge, W. Liu, J.F. Daigle, Y. Kamali, P. Simard, J. Bernhardt, S. Hoseinni, G. Méjean, A. Azarm, C. Marceau, O. Kosareva, V.P. Kandidov, N. Akozbek, A. Becker, G. Roy, P. Mathieu, J.R. Simard, M. Châteauneuf, J. Dubois, Filamentation 'remote' sensing of chemical and biological agents/pollutants using only one femtosecond laser. Appl. Phys. B **95**, 1 (2009)
11. M. Rodriguez, R. Bourayou, G. Méjean, J. Kasparian, J. Yu, E. Salmon, A. Scholz, B. Stecklum, J. Eislöffel, U. Laux, A.P. Hatzes, R. Sauerbrey, L. Wöste, J.-P. Wolf, Kilometer-range nonlinear propagation of femtosecond laser pulses. Phys. Rev. E **69**, 036607 (2004)
12. J.H. Marburger, Theory of self focusing. Prog. Quantum Electron. **4**, 35 (1975)
13. J. Kasparian, R. Sauerbrey, S.L. Chin, The critical laser intensity of self-guided light filaments in air. Appl. Phys. B **71**, 877 (2000)
14. A. Becker, N. Akozbek, K. Vijayalakshmi, E. Oral, C.M. Bowden, S.L. Chin, Intensity clamping and re-focusing of intense femtosecond laser pulses in nitrogen molecular gas. Appl. Phys. B **73**, 287–290 (2001)
15. P. Rairoux, H. Schillinger, S. Niedermeier, M. Rodriguez, F. Ronneberger, R. Sauerbrey, B. Stein, D. Waite, C. Wedekind, H. Wille, L. Wöste, Remote sensing of the atmosphere using ultrashort laser pulses. Appl. Phys. B **71**, 573 (2000)
16. S.A. Hosseini, Q. Luo, B. Ferland, W. Liu, S.L. Chin, O.G. Kosareva, N.A. Panov, N. Aközbek, V.P. Kandidov, Competition of multiple filaments during the propagation of intense femtosecond laser pulses. Phys. Rev. A **70**, 033802 (2004)
17. R. Ackermann, E. Salmon, N. Lascoux, J. Kasparian, P. Rohwetter, K. Stelmaszczyk, S. Li, A. Lindinger, L. Wöste, P. Béjot, L. Bonacina, J.-P. Wolf, Optimal control of filamentation in air. Appl. Phys. Lett. **89**, 171117 (2006)
18. G. Heck, J. Sloss, R.J. Levis, Adaptive control of the spatial position of white light filaments in an aqueous solution. Opt. Commun. **259**(1), 216 (2006)
19. T. Baumert, T. Brixner, V. Seyfried, M. Strehle, G. Gerber, Femtosecond pulse shaping by an evolutionary algorithm with feedback. Appl. Phys. B **65**(6), 779 (1997)
20. F. Théberge, W. Liu, P.Tr. Simard, A. Becker, S.L. Chin, Plasma density inside a femtosecond laser filament in air: Strong dependence on external focusing. Phys. Rev. E **74**, 036406 (2006)
21. W. Liu, F. Théberge, J.-F. Daigle, P.T. Simard, S.M. Sarifi, Y. Kamali, H.L. Xu, S.L. Chin, An efficient control of ultrashort laser filament location in air for the purpose of remote sensing. Appl. Phys. B **85**(1), 55 (2006)
22. G. Fibich, Y. Sivan, Y. Ehrlich, E. Louzon, M. Fraenkel, S. Eisenmann, Y. Katzir, A. Zigler, Control of the collapse distance in atmospheric propagation. Opt. Express. **14**(12), 4946–4957 (2006)
23. H. Wille, M. Rodriguez, J. Kasparian, D. Mondelain, J. Yu, A. Mysyrowicz, R. Sauerbrey, J.P. Wolf, L. Wöste, Teramobile: a mobile femtosecond-terawatt laser and detection system. Eur. Phys. J. A **20**, 183 (2002)
24. Z. Jin, J. Zhang, M.H. Xu, X. Lu, Y.T. Li, Z.H. Wang, Z.Y. Wei, X.H. Yuan, W. Yu, Control of filamentation induced by femtosecond laser pulses propagating in air. Opt. Express. **13**, 10424 (2005)
25. J.-F. Daigle, Y. Kamali, J. Bernhardt, W. Liu, C. Marceau, A. Azarm, S.L. Chin, Generation of powerful filaments at a long distance using adaptive optics. Opt. Commun. **281**, 3327 (2008)
26. Night N Adaptive Optics Ltd. (2009). http://www.nightn.ru/
27. R.K. Tyson, *Adaptive Optics Engineering Handbook* (Marcel Dekker, New York, 2000)

28. Laser interferometers Zygo (2009). http://zygo.com/?/met/interferometers/&gclid=COWt17GXvpgCFQMnGgodVzhobA
29. Schott UG11 transmission data sheet. Optical-Filters.com (2009). http://www.optical-filters.com/ug11.html
30. J.-F. Daigle, P. Mathieu, G. Roy, J.-R. Simard, S.L. Chin, Multi-constituents detection in contaminated aerosol clouds using remote filament-induced breakdown spectroscopy. Opt. Commun. **278**, 147 (2007)
31. C. Favre, V. Boutou, S.C. Hill, W. Zimmer, M. Krenz, H. Lambrecht, J. Yu, R.K. Chang, L. Wöste, J.-P. Wolf, White light nanosource with directional emission. Phys. Rev. Lett. **89**(3), 035002 (2002)
32. Q. Luo, S.A. Hosseini, W. Liu, J.-F. Gravel, O.G. Kosareva, N.A. Panov, N. Aközbek, V.P. Kandidov, G. Roy, S.L. Chin, Effect of beam diameter on the propagation of intense femtosecond laser pulses. Appl. Phys. B **80**, 35–38 (2005)